This is a repository copy of *Unraveling magnetic properties and martensitic transformation in Mn-rich Ni–Mn–Sn alloys: first-principles calculations and experiments*.

White Rose Research Online URL for this paper:
https://eprints.whiterose.ac.uk/212202/

Version: Accepted Version

Article:

Zhang, Y. orcid.org/0000-0001-7944-4947, Bai, J., Guo, K.-L. et al. (8 more authors) (2024) Unraveling magnetic properties and martensitic transformation in Mn-rich Ni–Mn–Sn alloys: first-principles calculations and experiments. Rare Metals, 43 (4). pp. 1769-1785. ISSN 1001-0521

https://doi.org/10.1007/s12598-023-02538-z

© 2024 The Authors. Except as otherwise noted, this author-accepted version of a journal article published in Rare Metals is made available via the University of Sheffield Research Publications and Copyright Policy under the terms of the Creative Commons Attribution 4.0 International License (CC-BY 4.0), which permits unrestricted use, distribution and reproduction in any medium, provided the original work is properly cited. To view a copy of this licence, visit http://creativecommons.org/licenses/by/4.0/

Reuse

This article is distributed under the terms of the Creative Commons Attribution (CC BY) licence. This licence allows you to distribute, remix, tweak, and build upon the work, even commercially, as long as you credit the authors for the original work. More information and the full terms of the licence here: https://creativecommons.org/licenses/

Takedown

If you consider content in White Rose Research Online to be in breach of UK law, please notify us by emailing eprints@whiterose.ac.uk including the URL of the record and the reason for the withdrawal request.

eprints@whiterose.ac.uk
https://eprints.whiterose.ac.uk/

Investigation on magnetic properties, martensitic transformation, and kinetics of Ni-Mn-Sn alloys with excess Mn: first-principles calculations and experiments

Yu Zhang[1,2], Jing Bai[1,2,4] *, Keliang Guo[1], Jiaxin Xu[1,2], Jianglong Gu[3], Nicola Morley[4], Qiuzhi Gao[2], Yudong Zhang[5], Claude Esling[5], Xiang Zhao[1], Liang Zuo[1]

[1]Key Laboratory for Anisotropy and Texture of Materials (Ministry of Education), School of Material Science and Engineering, Northeastern University, Shenyang 110819, China

[2]Key Laboratory of Dielectric and Electrolyte Functional Material Hebei Province, School of Resources and Materials, Northeastern University at Qinhuangdao, Qinhuangdao 066004, PR China

[3]State Key Laboratory of Metastable Materials Science and Technology, Yanshan University, Qinhuangdao 066004, China

[4]Department of Material Science and Engineering, University of Sheffield, Sheffield, S1 3JD, UK

[5]Laboratoire d'Étude des Microstructures et de Mécanique des Matériaux, UMR 7239, LEM3, CNRS, University of Lorraine, 57045 Metz, France

*Corresponding author: baijing@neuq.edu.cn

ABSTRACT

We have investigated the phase stability, magnetic properties, martensitic transformation, and kinetics of the $Ni_{24-x}Mn_{18+x+y}Sn_{6-y}$ (x, y=0, 1, 2) system by combining the first-principles calculations and experiments. The calculation results show that the optimized lattice parameters are consistent with the experimental data. Respectively obtain the relation equation of austenite formation energy ($E_{form\text{-}A}$) and Mn content (X_{Mn}): $E_{form\text{-}A}=507.358X_{Mn}-274.126$, and the relation equation of six-layer modulated (6M) martensite formation energy ($E_{form\text{-}6M}$) and Ni content (X_{Ni}): $E_{form\text{-}6M}=-728.484X_{Ni}+264.374$. The stable magnetic state of each phase is determined by the lowest formation energy (E_{form}), and the ternary phase diagram of total magnetic moment is established. Excessive Mn will reduce the total magnetic moment of 6M (Mag_{6M}) and non-modulated (NM) (Mag_{NM}) martensites, with the following equations relating the total magnetic moment and Mn content: $Mag_{6M}=-15.905X_{Mn}+7.902$ and $Mag_{NM}=-14.781X_{Mn}+7.411$, while the effect on austenite is complex. The Mn atomic magnetic moment is not only the primary contributor to the total magnetic moment, but also the dominant driver of the trend in the total magnetic moment. Based on the thermodynamics of martensitic transformation, the alloys will likely undergo Austenite↔6M↔NM transformation sequence. Combining the thermodynamic and kinetic results, the martensitic transformation temperature decreases with increasing x and increases with increasing y. The 3d electrons of Mn_{Sn} (Mn at Sn sublattice) play an important role in magnetic properties as revealed by the electronic density of states. These results are expected to provide reference for predicting the phase stability and magnetic properties of Ni-Mn-Sn alloys.

Keywords**:** Ni-Mn-Sn; First-principles calculations; Martensitic transformation; Magnetic property; Kinetics

1. Introduction

Heusler-type Ni-Mn-X (X=In, Sn, and Sb) metamagnetic shape memory alloys (MSMAs) have attracted significant attention owing to their multifunctional properties, such as magnetic shape memory effect (MSME)[1,2], magnetocaloric effect (MCE)[3,4], elastocaloric effect (eCE)[5,6], and magnetoresistance (MR)[7,8]. Essentially, all these excellent functional behaviors originate from the martensitic transformation (MT) involving coupled structural and magnetic transition. In particular, Ni-Mn-Sn alloys have the advantages of rare-earth-free, low-cost, and environmental protection. These excellent comprehensive performances have great application potential in aerospace, communication, information, room-temperature refrigeration, and other fields[9].

The high-temperature austenitic structure of Ni-Mn-Sn alloys has been proven to be the cubic $L2_1$ structure, while the low-temperature martensitic structure can exist in multiple possibilities [10,11]. The martensite can be divided into modulated martensite and NM martensite. The modulated martensite includes four-layered orthorhombic (4O), five-layer modulated (5M), 6M, and seven-layer modulated (7M) types mainly depending on the chemical composition.

It has been widely recognized that the excellent properties of MSMAs are due to the existence of modulated martensite. Zhang *et al.*[12] demonstrated giant elastocaloric and magnetocaloric effects in the textured $Ni_{43}Mn_{47}Sn_{10}$ alloy, which undergo the MT from a $L2_1$ structure at 298K to a 6M martensite structure at 253K measured by powder X-ray diffraction (XRD). Huang *et al.*[13] reported that the polycrystalline $Ni_{41}Co_9Mn_{40}Sn_{10}$ alloy exhibits a large magnetic entropy change ($\triangle S_M$) of 31.9 J·kg^{-1}·K^{-1} and a significant MR of 53.8% under a 5 T magnetic field. Subsequently, the existence of 6M martensite was found at 100K by in-situ synchrotron high-energy XRD, and the selected area electron diffraction pattern of 6M martensite was confirmed using transmission electron microscopy (TEM) at room temperature. Li *et al.*[14] proved that a giant recoverable strain of about 20% along $<001>_A$ can be obtained in $Ni_{50}Mn_{31.4}Sn_{9.6}Fe_9$ magnetic microwire, which is related to the stress-induced $L2_1 \rightarrow 6M \rightarrow NM$ two-step MT. Overall, these large $\triangle S_M$, MR, and recoverable strain are also attributed to the presence of 6M martensite in Ni-Mn-Sn-based alloys. Despite the common occurrence of 6M martensite in Ni-Mn-Sn alloy, current research has mostly focused on specific compositions in experiments[15-17]. Due to the complexity of its long-period amplitude modulation structure and lack of accurate atomic positions, the simulation calculation of the modulated structure is challenging, so current theoretical studies have primarily focused on austenite and NM martensite. Since the austenite in the Ni-Mn-Sn and Ni-Mn-In systems is completely ordered and the MT is non-diffusive[18], the phase stability and magnetic properties of 6M martensite in the Ni-Mn-Sn system can be calculated with the help of crystal structure and atomic occupation of 6M martensite which has been accurately analyzed in the Ni-Mn-In system[19]. The metastable modulated martensite eventually tends to transform into the stable NM martensite with decreasing temperature[14,20], thus, we aim to explore the MT sequence including 6M martensite by using the first-principles calculations.

At present, the martensitic transformation temperature (T_M) can be adjusted over a wide range by changing the non-stoichiometric concentration or by doping other elements, providing a large design space. It is crucial to find a predictor to accurately predict the relationship between composition and T_M. The number of valence electrons per atom (*e*/*a*) has been commonly used as a predictor[21], but it is not always applicable[22-24]. Furthermore, Li *et al.*[25] proposed that shear elastic modulus (C') is more accurate in predicting T_M than *e*/*a*, but Luo *et al.*[26] found that the C'–T_M relation breaks down for the $Ni_2(Mn_{1-x}Fe_x)Ga$ alloys. The above-mentioned parameters *e*/*a* and C' are only related to the properties of the austenite while ignoring the properties of the martensite, although both the austenite and martensite participate in the MT. Therefore, considering the energy difference ($\triangle E$) between austenite and martensite can determine T_M qualitatively by taking into account the properties of both phases. It is well known that there are two decisive factors for the occurrence of MT. On the one hand, it is necessary to provide the free energy difference between the austenite and martensite, that is, the phase transition driving force. Another aspect is that it is essential to overcome the phase transformation barrier during the lattice deformation of the phase transition, that is, the phase transition activation energy (Q)[27]. The greater the $\triangle E$, the larger the driving force for phase transformation, resulting in an increase in phase transition temperature. Additionally, the phase transition barrier is getting larger with increasing Q, making the phase transformation more difficult and increasing the corresponding phase transition temperature[28]. Therefore, this paper combines phase transformation thermodynamics (first-principles calculations) and non-isothermal kinetics (experiments) to investigate the root cause of T_M variation with composition, providing guidance for the design of Ni-Mn-Sn alloy.

As known, the first-principles calculations can serve as an efficient and accurate tool for predicting the phase stability and magnetic properties of different compositions, and experiments can verify the accuracy of theoretical calculations. Based on these preconditions, we addressed the following issues: first, changes in formation energy and magnetic moment are projected onto the ternary phase diagrams, and the relations between these properties and composition in each phase are obtained respectively. Second, the MT path of the $Ni_{24-x}Mn_{18+x+y}Sn_{6-y}$ system is determined. Third, the relation between the martensitic transformation temperature and composition was revealed through a combination of thermodynamics and kinetics. These findings provide valuable information for the further design and development of Ni-Mn-based alloys.

2. Computational and experimental details

All calculations were based on the spin-polarized density functional theory (DFT) as implemented in the Vienna ab initio Simulation Package (VASP)[29,30]. The projector-augmented wave (PAW) pseudopotential approach was used to describe the interaction between ions and electrons[31,32]. The Perdew-Burke-Ernzerhof implementation of generalized gradient approximation (PBE-GGA) approach was employed to treat the exchange-correlation functional[33]. Valence electron configurations used for Ni, Mn, and Sn were $3d^8 4s^2$, $3d^6 4s^1$, and $4d^{10} 5s^2 5p^2$, respectively. Fig. 1 shows the crystal structures of $L2_1$ austenite (Fig. 1(a)), NM (Fig. 1(b)), 4O (Fig. 1(c)), and 6M (Fig. 1(d)) martensites with 16, 8, 16, and 24 atoms per unit cell, respectively. To facilitate the comparison, a 48-atoms supercell was constructed. The austenite, NM, 4O, and 6M martensites used Monkhorst-Pack 12×12×4, 7×10×11, 3×13×17, and 8×13×6 *k*-points for the first Brillouin zone sampling, respectively[34]. The structural relaxation was performed with a plane-wave cutoff energy of 351eV, and the convergence criteria for total energy, force, and external pressure were set to be 10^{-4} eV, 0.02 eV/A, and ± 3 kB, respectively. Detailed crystallographic information on 6M and 4O martensites is available from Ref. [19] and Ref. [35], respectively.

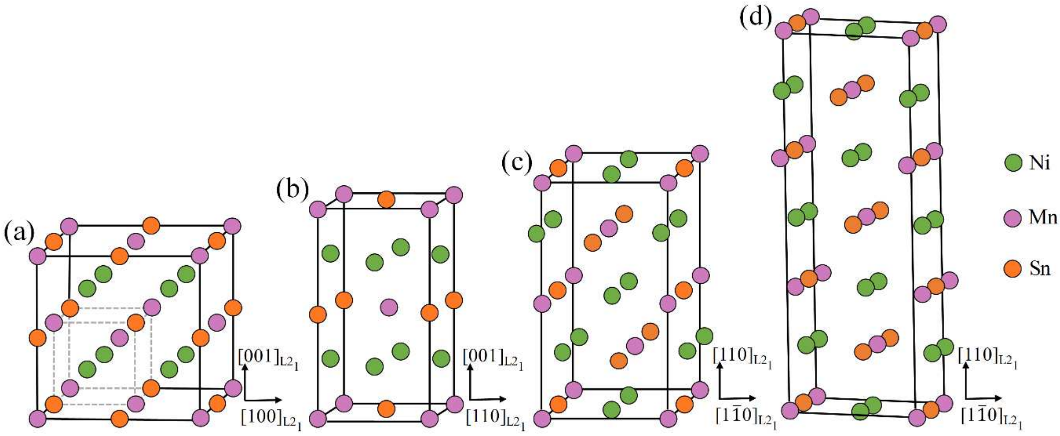

Fig. 1. Crystal structures of (a) $L2_1$ austenite, (b) NM, (c) 4O, and (d) 6M martensites for Ni_2MnSn per unit cell.

In this work, we investigated the optimal magnetic configuration and phase stability of each phase in the $Ni_{24-x}Mn_{18+x+y}Sn_{6-y}$ system, the formation energy (E_{form}) was calculated using Eq. (2-1)[36].

$$E_{\mathrm{form}} = \frac{E_{\mathrm{total}}(\mathrm{Ni}_{24-x}\mathrm{Mn}_{18+x+y}\mathrm{Sn}_{6-y}) - (24-x)E_{\mathrm{Ni}} - (18+x+y)E_{\mathrm{Mn}} - (6-y)E_{\mathrm{Sn}}}{48} \times 1000 \qquad (2\text{-}1)$$

where E_{total} is the total ground-state energy of the compound; E_{Ni}, E_{Mn}, and E_{Sn} represent the ground-state energy per atom of Ni (face-centered cubic structure, ferromagnetic), Mn (complex body-centered cubic structure, ferromagnetic), and Sn (diamond cubic structure, paramagnetic) pure elements in their reference bulk states, and $24-x$, $18+x+y$, and $6-y$ are the numbers of Ni, Mn, and Sn in the 48-atom supercell, respectively. The lower E_{form} corresponds to the higher phase stability.To verify the calculation results, a series of non-textured polycrystalline $Ni_{24-x}Mn_{18+x+y}Sn_{6-y}$ (x, y=0, 1, 2) alloys were prepared by arc melting of high purity (99.99%) elements under the argon atmosphere protection. To eliminate compositional segregation, the as-cast ingots were further homogenized at 1173K for 48h in a vacuum condition and quenched in cold water. The actual composition was verified by energy dispersive spectrometry (EDS, JSM-7001F). The room-temperature crystal structure was analyzed by XRD (Rigaku SMARTLAB 9) with Cu Kα radiation after annealing the powder samples at 873 K for 5 h. The start and finish temperatures for the forward and reverse martensitic transformations (M_f, M_s, A_f, and A_s) were analyzed by differential scanning calorimetry (DSC, TA-Q100) measurements with heating and cooling rates of 10 K/min. DSC with different heating rates from 5 to 20 K/min was used to explain the root cause of the T_M change with composition from the perspective of non-isothermal kinetics. Selected area electron diffraction pattern was observed by TEM (JEM-2100F) to further determine the room-temperature crystal structure.

3. Results and discussion

3.1. Magnetic configuration and phase stability

To analyze the magnetic configuration in detail, both ferromagnetic (FM) and ferrimagnetic (FIM) states were considered. Especially in the bivariate $Ni_{24-x}Mn_{18+x+y}Sn_{6-y}$ ($x\neq0$) system, three ferrimagnetic states were investigated, as demonstrated by Fig. 2. The magnetic moments of normal Mn (Mn_{Mn}) atoms and excess Mn atoms are parallel, denoted as FM, as shown in Fig. 2(a), (c) and (e). In the univariate $Ni_{24}Mn_{18+y}Sn_{6-y}$ (x=0) system, the magnetic moment of Mn_{Mn} atoms is antiparallel to that of Mn_{Sn}, denoted as FIM, depicted in Fig. 2(d). When excess Mn atoms occupy both Sn and Ni sites (Mn_{Ni}), “FIM1” represents that the magnetic moment directions for all excess Mn atoms are antiparallel to that of the Mn_{Mn} atoms, as displayed in Fig. 2(f). If the magnetic moment direction of Mn_{Ni} or Mn_{Sn} atoms arranged anti-parallel to that of Mn_{Mn} atoms, they are named “FIM2” or “FIM3”, respectively, as seen in Fig. 2(g) and (h).

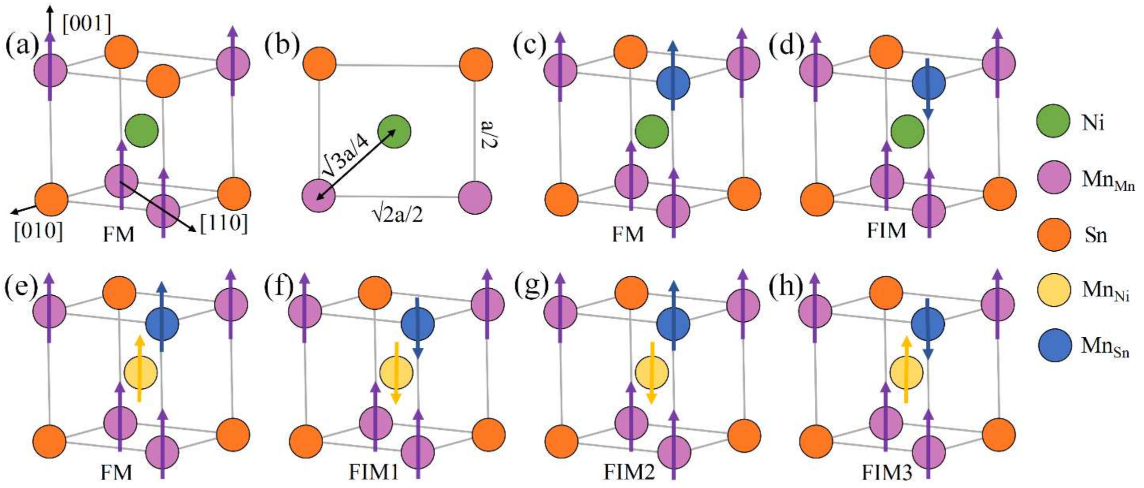

Fig. 2. Unit cell of $L2_1$ structure: (a) Magnetic moment distribution diagram and (b) atomic distribution of (110) plane of $Ni_{24}Mn_{12}Sn_{12}$ alloy; (c) FM and (d) FIM coupling between Mn_{Mn} and Mn_{Sn} in $Ni_{24}Mn_{18+y}Sn_{6-y}$ (x=0) alloys; (e) FM and (f) FIM1 coupling between Mn_{Mn} and excess Mn, (g) FIM2 and (h) FIM3 indicate magnetic moment direction of Mn_{Ni} or Mn_{Sn} arranges anti-parallel to that of Mn_{Mn} in $Ni_{24-x}Mn_{18+x+y}Sn_{6-y}$ ($x\neq0$) alloys.

Fig. 3 shows the E_{form} of the austenite, 6M, and NM martensites for the $Ni_{24-x}Mn_{18+x+y}Sn_{6-y}$ (x, y=0, 1, 2) alloys in both ferromagnetic and ferrimagnetic states. The austenite's magnetic configuration dependence on the composition shows complexity within the studied range. The E_{form}

of the austenite in the FIM state is lower than that in the FM state for x=0, indicating that the austenite exists stably in the FIM state for the $Ni_{24}Mn_{18+y}Sn_{6-y}$ alloys. For the $Ni_{24-x}Mn_{18+x+y}Sn_{6-y}$ (x=1 and 2) alloys, the E_{form} of austenite in the FIM2 state is the lowest. Remarkably, the FM state is extremely unstable, transforming spontaneously into the most stable FIM2 state during the structural optimization. Exchange interactions between Mn atoms strongly depend on the nearest Mn-Mn distance. In the Sn-deficient alloys, excess Mn atoms couple antiferromagnetically to Mn_{Mn} atoms, as the Mn_{Sn}-Mn_{Mn} distance ((1/2)a) is closer than that between normal Mn atoms (($\sqrt{2}/2$)a) (see Fig. 2(b) and (d)). However, for the alloys deficient in both Ni and Sn, the Mn_{Mn}-Mn_{Ni} distance (($\sqrt{3}/4$)a) is closer than Mn_{Mn}-Mn_{Sn} distance ((1/2)a). Therefore, the antiferromagnetic coupling between Mn_{Mn} and Mn_{Ni} atoms is stronger than that between Mn_{Mn} and Mn_{Sn} atoms. Additionally, both Mn_{Mn} and Mn_{Sn} atoms have the same distance from Mn_{Ni} atom and couple antiferromagnetically to the Mn_{Ni} atom. Hence, the ferromagnetic coupling between Mn_{Mn} and Mn_{Sn} atoms established (see Fig.2 (g)). Consequently, the FIM2 state of austenite is the most thermodynamically stable in the $Ni_{24-x}Mn_{18+x+y}Sn_{6-y}$ (x=1 and 2) system.

Nevertheless, the magnetic configuration of martensite is not affected by composition. For the 6M and NM martensites, the E_{form} of the FIM and FIM1 states is the lowest in $Ni_{24}Mn_{18+y}Sn_{6-y}$ (x=0) and $Ni_{24-x}Mn_{18+x+y}Sn_{6-y}$ (x=1, 2) alloys, where the spin directions of the magnetic moments for the excess Mn atoms are aligned antiparallel to that of the normal Mn atoms. Previous study shows that reducing the Mn-Mn distance below the critical value of about 3Å changes the magnetic interaction from ferromagnetic to antiferromagnetic[37]. In the optimized structures of 6M and NM martensites, the distances between the nearest neighboring Mn_{Mn}-Mn_{Ni} and Mn_{Mn}-Mn_{Sn} are less than 3Å, favoring the stabilization of the antiferromagnetic state. Therefore, the FIM and FIM1 states are the most thermodynamically stable states of the 6M and NM martensites for the $Ni_{24}Mn_{18+y}Sn_{6-y}$ (x=0) and $Ni_{24-x}Mn_{18+x+y}Sn_{6-y}$ (x=1, 2) alloys, respectively.

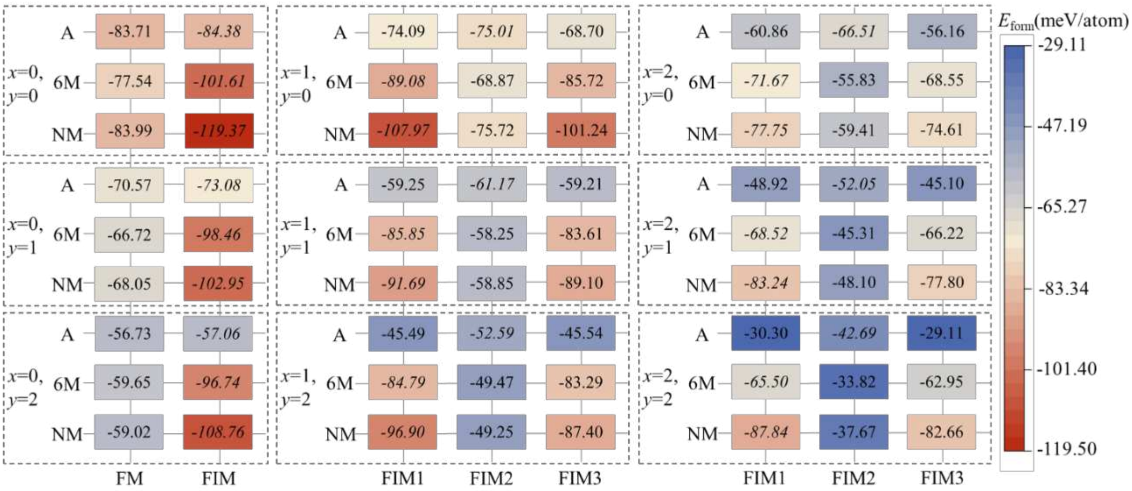

		FM	FIM
x=0, y=0	A	-83.71	*-84.38*
	6M	-77.54	*-101.61*
	NM	-83.99	*-119.37*
x=0, y=1	A	-70.57	*-73.08*
	6M	-66.72	*-98.46*
	NM	-68.05	*-102.95*
x=0, y=2	A	-56.73	*-57.06*
	6M	-59.65	*-96.74*
	NM	-59.02	*-108.76*

		FIM1	FIM2	FIM3
x=1, y=0	A	-74.09	*-75.01*	-68.70
	6M	*-89.08*	-68.87	-85.72
	NM	*-107.97*	-75.72	-101.24
x=1, y=1	A	-59.25	*-61.17*	-59.21
	6M	*-85.85*	-58.25	-83.61
	NM	*-91.69*	-58.85	-89.10
x=1, y=2	A	-45.49	*-52.59*	-45.54
	6M	*-84.79*	-49.47	-83.29
	NM	*-96.90*	-49.25	-87.40

		FIM1	FIM2	FIM3
x=2, y=0	A	-60.86	*-66.51*	-56.16
	6M	*-71.67*	-55.83	-68.55
	NM	*-77.75*	-59.41	-74.61
x=2, y=1	A	-48.92	*-52.05*	-45.10
	6M	*-68.52*	-45.31	-66.22
	NM	*-83.24*	-48.10	-77.80
x=2, y=2	A	-30.30	*-42.69*	-29.11
	6M	*-65.50*	-33.82	-62.95
	NM	*-87.84*	-37.67	-82.66

Fig. 3. E_{form} of A, 6M, and NM phases in ferromagnetic and ferrimagnetic states for $Ni_{24-x}Mn_{18+x+y}Sn_{6-y}$ (x, y=0, 1, 2) alloys. Italic indicates the lowest E_{form} for each phase of alloys.

Subsequently, we project the formation energies of the austenite, 6M, and NM phases with the most stable magnetic configuration onto the ternary phase diagram, as illustrated in Fig. 4. The contour lines in Fig. 4(a) reveal that the E_{form} of austenite increases gradually with the Mn content increases, leading to a decrease in the stability of austenite. As displayed by the black scattered points and line in Fig. 4(d), based on the current calculation results, the $E_{form\text{-}A}$ and the X_{Mn} in the alloy are linearly fitted, and the fitting equation is obtained and shown in Eq. 3-1. Furthermore, Fig. 4(b) displays that the stability of 6M increases with increasing Ni content, as the bright region with higher E_{form} gradually transfers to the blue region with lower E_{form}. Thus, we obtained a fitting equation (Eq. 3-2) between the X_{Ni} and the $E_{form\text{-}6M}$ martensite, as shown by the red fitted line in Fig. 4(d). From Fig. 4(c), with the same Sn content, the E_{form} of NM martensite is higher as more Ni sites are substituted by Mn.

$$E_{form\text{-}A}=507.358X_{Mn}-274.126 \tag{3-1}$$

$$E_{form\text{-}6M}=-728.484X_{Ni}+264.374 \tag{3-2}$$

Where $E_{form\text{-}A}$ and $E_{form\text{-}6M}$ are the formation energies of austenite and 6M martensite, respectively. X_{Mn} and X_{Ni} represent the Mn and Ni proportions in the alloy, respectively. The ternary phase stability diagrams and the fitting equations can conveniently predict the E_{form} of each phase for various compositions, thereby enabling the prediction of phase stability without the need for numerous complicated experiments to screen compositions. It provides a more simple and direct approach for designing the alloy composition.

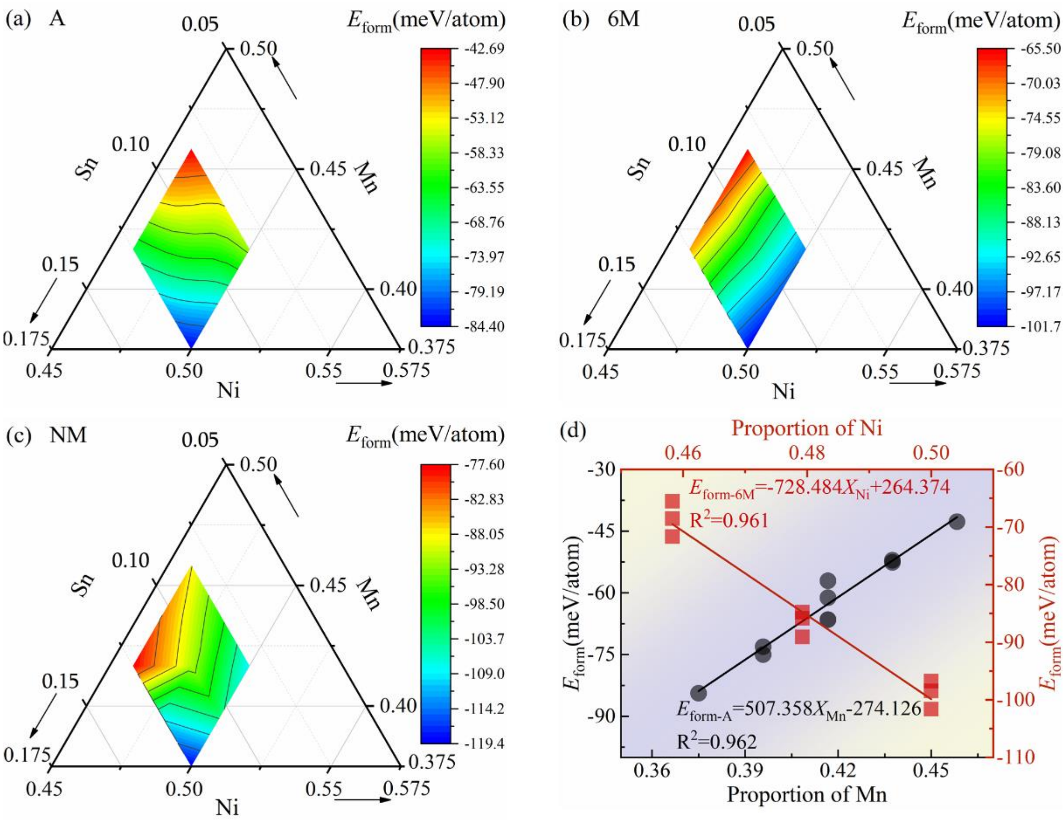

Fig. 4. Mapping of E_{form} on ternary phase diagram of $Ni_{24-x}Mn_{18+x+y}Sn_{6-y}$ alloys: (a) A, (b) 6M, and (c) NM phases, (d) A diagram of relationship between E_{form} and composition.

3.2. Optimized structural parameters and magnetic properties

The optimized lattice parameters and volume per formula unit of the austenite, 6M, and NM martensites for the $Ni_{24-x}Mn_{18+x+y}Sn_{6-y}$ system are depicted in Table 1. The lattice parameter *a* of austenite decreases and the unit cell volume (*V*) shrinks with Mn_{Sn} content *y* increases when Mn_{Ni} content *x* remains constant, and vice versa. The atomic radius difference is the primary factor affecting the change in lattice parameters (the atom radii are 1.25Å for Ni, 1.35Å for Mn, and 1.63Å for Sn, respectively). For the 6M martensite, there is no obvious rule between *a* and composition, while *b*, *c*, and *V* gradually decrease, and *β* increases as Mn_{Sn} content *y* increases. For the NM martensite, *a* decreases and *c* increases with the increase of *y* when *x* remains constant, resulting in a shrink in *V*. However, when Mn_{Sn} content *y* is constant, *a* decreases, *c* increases, and *V* expands with the increase in Mn_{Ni} content *x*. The change in lattice constant is the same, but the volume change is the opposite. Despite a slight deviation between the experimental and calculated values, they are generally in good agreement. This can be attributed to two factors: First, the experimental compositions are not precisely the same as the calculated compositions. Furthermore, the XRD test is carried out at room temperature, and the calculation is based on 0 K.

Table 1 Optimized lattice parameters and volume per formula unit of $Ni_{24\text{-}x}Mn_{18+x+y}Sn_{6\text{-}y}$ alloys (Bold italic represents the experimental value).

Phase	Lattice parameters	$x = 0$			$x = 1$			$x = 2$		
		$y = 0$	$y = 1$	$y = 2$	$y = 0$	$y = 1$	$y = 2$	$y = 0$	$y = 1$	$y = 2$
A	$a = b = c$ (Å)	5.926	5.901	5.890	5.950	5.932	5.915	5.953	5.936	5.915
		–	–	–	***5.978***	–	–	***5.997***	–	–
	V (Å^3)	52.038	51.375	51.088	52.669	52.186	51.726	52.751	52.279	51.730
6M	a (Å)	4.427	4.430	4.442	4.458	4.458	4.452	4.477	4.456	4.446
		–	***4.421***	***4.420***	–	***4.421***	***4.414***	–	***4.415***	***4.435***
	b (Å)	5.455	5.382	5.319	5.416	5.365	5.301	5.406	5.370	5.316
		–	***5.537***	***5.480***	–	***5.557***	***5.484***	–	***5.574***	***5.488***
	c (Å)	12.863	12.824	12.774	12.878	12.850	12.796	12.856	12.836	12.775
		–	***12.998***	***12.955***	–	***12.997***	***12.950***	–	***12.996***	***12.990***
	β (°)	94.431	94.847	95.163	94..636	95.021	95.362	94.259	94.032	95.017
		–	***93.596***	***94.237***	–	***93.222***	***94.154***	–	***93.203***	***93.345***
	V (Å^3)	51.606	50.776	50.097	51.518	51.032	50.115	51.718	51.066	50.133
NM	$a = b$ (Å)	3.770	3.767	3.720	3.812	3.750	3.713	3.806	3.751	3.708
	c (Å)	7.194	7.123	7.181	7.091	7.180	7.220	7.125	7.211	7.256
	V (Å^3)	51.122	50.514	49.687	51.518	50.514	49.764	51.616	50.729	49.883

To reveal the variation of the total magnetic moment and magnetization difference ($\triangle M$) with composition in the $Ni_{24\text{-}x}Mn_{18+x+y}Sn_{6\text{-}y}$ alloys, we calculated the total magnetic moment of each phase, as shown in Fig. 5. The total magnetic moment of each phase in the FIM state decreases with the increase in Mn_{Sn} content y for the $Ni_{24}Mn_{18+y}Sn_{6\text{-}y}$ (x=0) alloys. Furthermore, the difference in magnetization between different phases is slight for the same composition, and the $\triangle M$ remains almost unchanged with the composition during (inter)martensitic transformation.

For the $Ni_{24\text{-}x}Mn_{18+x+y}Sn_{6\text{-}y}$ ($x\neq0$) system, the total magnetic moment of austenite increases with Mn_{Sn} content y and decreases with Mn_{Ni} content x. However, the magnetic moments of 6M and NM martensites have little difference, both decrease with the increase in x or y. It is worth mentioning that this series of alloys can produce a large $\triangle M$ when MT occurs. The $\triangle M$ exhibits a positive correlation with respect to y and remains relatively stable with changes in x. The larger $\triangle M$ is favorable to obtain a significant magnetic driving force (Zeeman Energy $E_{Zeeman}=\mu_0\triangle M$H) during the MT, which is a prerequisite for the realization of magnetostrictive shape memory alloys[38]. This explains why most experiments were compositionally tuned by adjusting Mn to replace Ni and Sn[12,39].

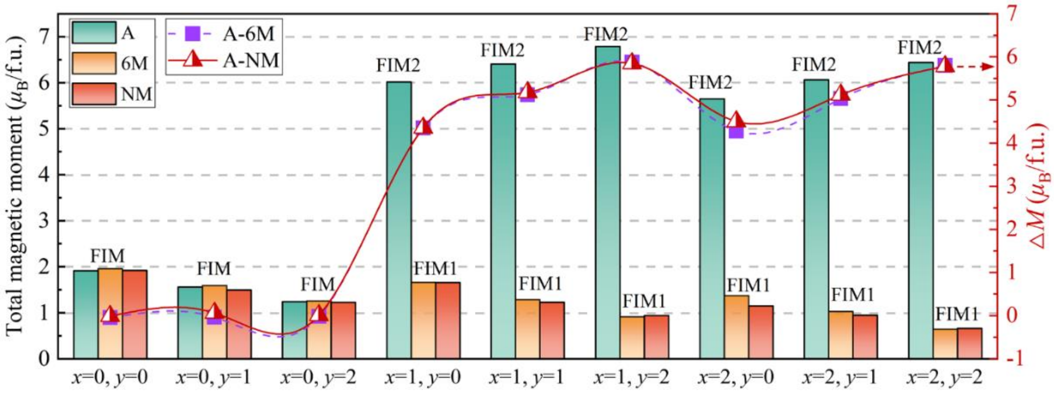

Fig. 5. Total magnetic moment per formula unit of austenite, 6M, and NM martensites as well as △M of A-6M and A-NM in $Ni_{24\text{-}x}Mn_{18+x+y}Sn_{6\text{-}y}$ (x, y=0, 1, 2) system.

Subsequently, we projected the total magnetic moment of each phase onto the ternary phase diagram in Fig. 6, to predict the total magnetic moment of alloys within a broader composition range. The trend of the total magnetic moment between austenite and martensite differs significantly, while that between 6M and NM martensites is very similar. For the austenite in Fig. 6(a), the maximum total magnetic moment occurs in the Mn-excess Ni and Sn-deficient alloys, and the minimum magnetic moment occurs in the alloy with 50% Ni content. As shown in Fig. 6(b) and (c), the maximum total magnetic moment of 6M and NM martensites occurs in alloys with lower Mn content. Additionally, as depicted in the upper right corner of the diamond projection in the phase diagram of Figure 6(a)-(c), the MT of the alloy in this composition region can produce a large △M. Furthermore, the total magnetic moment of 6M and NM martensites decreases with increasing Mn content. As shown in Fig. 6(d), we have fitted the relationship between the Mn content and the total magnetic moment of 6M and NM martensites and obtained their respective equations (Eq. 3-3 and Eq. 3-4).

$$\mathrm{Mag}_{6M}=-15.905X_{Mn}+7.902 \tag{3-3}$$

$$\mathrm{Mag}_{NM}=-14.781X_{Mn}+7.411 \tag{3-4}$$

Where Mag_{6M} and Mag_{NM} are the total magnetic moment of 6M and NM martensites, respectively. X_{Mn} represents the proportion of Mn in the alloy. The establishment of the ternary phase diagram of the total magnetic moment and the fitting of the relationship between the total magnetic moment and composition for martensites provide a theoretical foundation for composition design and selection.

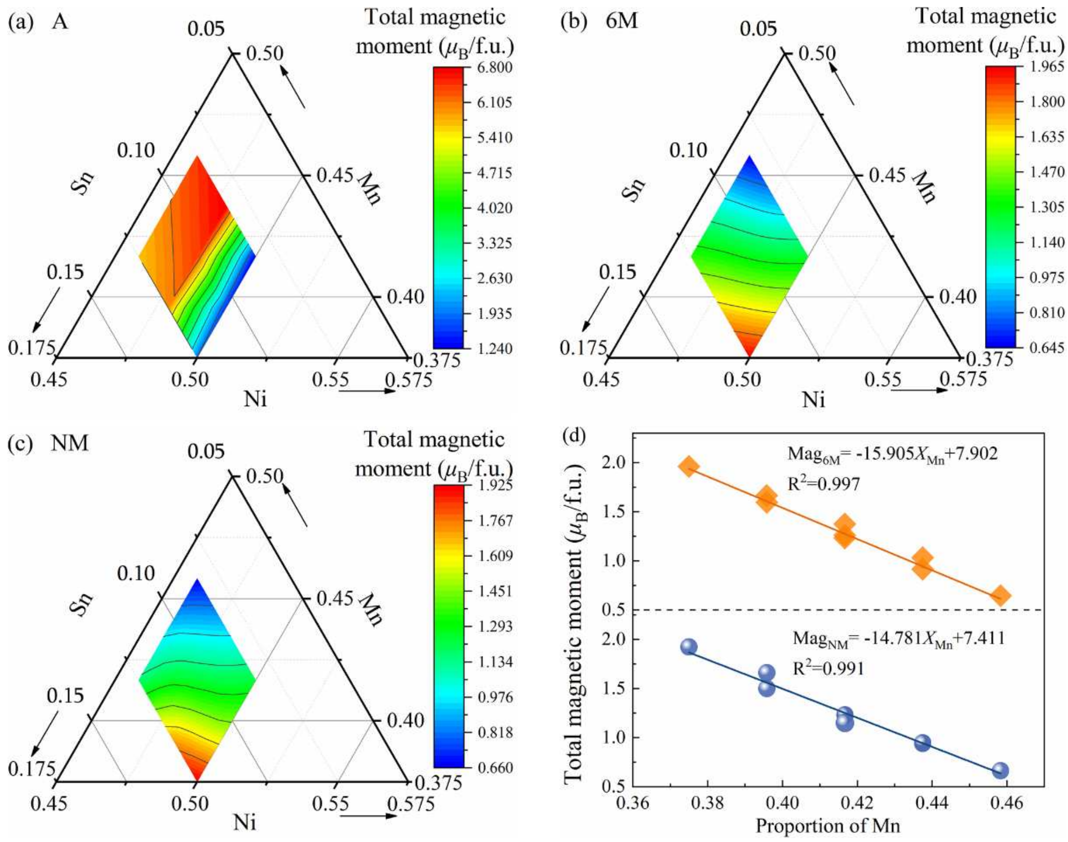

Fig. 6. Mapping of total magnetic moment (Mag) on ternary phase diagram of $Ni_{24-x}Mn_{18+x+y}Sn_{6-y}$ alloys: (a) A, (b) 6M, and (c) NM phases, (d) A diagram of relationship between total magnetic moment and composition.

To further reveal the contribution of each atom to the total magnetic moment of the $Ni_{24-x}Mn_{18+x+y}Sn_{6-y}$ alloys, the atomic magnetic moments of Ni and Mn are displayed in this section, as shown in Fig. 7. Since the Sn moment only varies between -0.022~-0.094 μ_B, the calculated result is consistent with previous study[40], the contribution of Sn moment to the total magnetic moment is ignored. The variation trends of the Ni moments are basically consistent with that of the total magnetic moments in the A and 6M phases. However, there are outliers in the NM martensite, the variation law of the Ni moments is not consistent with that of the total magnetic moment. The Mn is the main contributor to the total magnetic moment, and its moments in the austenite, 6M, and NM phases exhibit the same trend as the total magnetic moment. Thus, it can be concluded that the variation of total magnetic moment is mainly dominated by the average magnetic moment of Mn atoms.

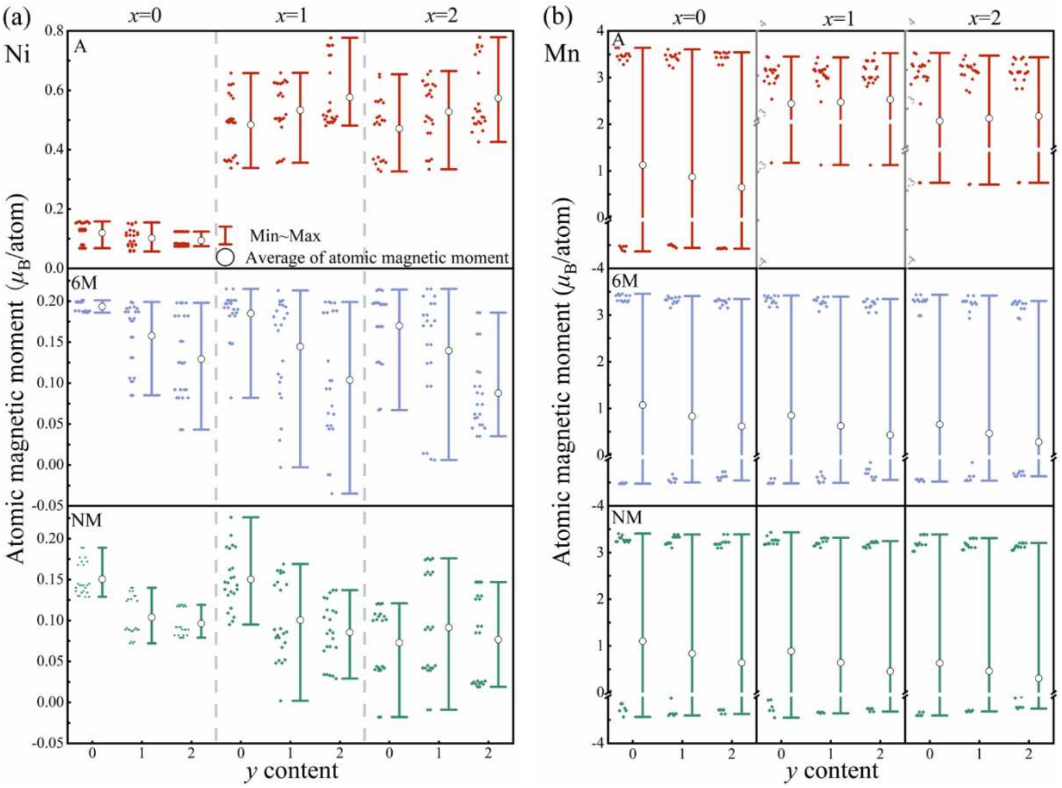

Fig. 7. Atomic magnetic moment of (a) Ni and (b) Mn atoms for $Ni_{24-x}Mn_{18+x+y}Sn_{6-y}$ system.

3.3. Thermodynamic behavior of martensitic transformation

Fig. 8 shows the variation of Mn_{Ni} content x and Mn_{Sn} content y on the E_{form} and $\triangle E$ of each phase, as well as the effect of Mn content on MT. From Fig. 8(a), the E_{form} of the FIM state austenite in $Ni_{24-x}Mn_{18+x+y}Sn_{6-y}$ (x=0) alloys and the FIM2 state austenite in $Ni_{24-x}Mn_{18+x+y}Sn_{6-y}$ (x=1 and 2) alloys both increases with the increase in Mn_{Ni} content x and Mn_{Sn} content y, implying that substituting Mn for Ni and Sn can destabilize austenite and potentially promote MT.

For the 6M martensite, the variation of E_{form} with Mn_{Ni} content x and Mn_{Sn} content y is similar to that for the austenite. For the NM martensite, the E_{form} changes with y without obvious regularity at x=0 and 1, but decreases with increasing y at x=2. When Mn_{Sn} content y remains constant, the E_{form} increases gradually with an increase in Mn_{Ni} content x. Interestingly, the E_{form} variation of the austenite and 6M martensite with Mn_{Ni} content x is consistent with that observed for the NM martensite, suggesting that increasing Mn_{Ni} content will render all three phases unstable. The E_{form} of different phases of any composition in Fig. 8(a) is from high to low: A→6M→NM, indicating that the alloy may undergo an intermartensitic transformation from high-temperature austenite to 6M martensite, with the latter then transforming into NM martensite as the temperature decreases. In summary, the possible martensitic transformation sequences are as follows:

$\text{Austenite}^{FIM}\rightarrow 6\text{M}^{FIM}\rightarrow \text{NM}^{FIM}$ ($Ni_{24\text{-}x}Mn_{18+x+y}Sn_{6\text{-}y}$ (x=0) alloys) and $\text{Austenite}^{FIM2}\rightarrow 6\text{M}^{FIM1}\rightarrow \text{NM}^{FIM1}$ ($Ni_{24\text{-}x}Mn_{18+x+y}Sn_{6\text{-}y}$ (x=1, 2) alloys).

From the perspective of phase transformation thermodynamics, MT requires a driving force, which arises from the △E between the new phase (martensite) and the parent phase (austenite). The likelihood of MT increases with a larger △E, resulting in a higher T_M. Fig. 8(b) shows that a positive △$E_{A\text{-}6M}$ value predicts a transformation from austenite to 6M martensite throughout the studied composition range. The △$E_{A\text{-}6M}$ ascends rapidly with an increase of Mn_{Sn} content y, indicating an enhanced driving force for MT. Therefore, as Mn_{Sn} content increases, T_M is proportional to Mn_{Sn} content y in the $Ni_{24\text{-}x}Mn_{18+x+y}Sn_{6\text{-}y}$ system. In addition, △$E_{A\text{-}6M}$ decreases rapidly with an increase in Mn_{Ni} content x, indicating that the driving force of MT decreases gradually, so T_M is inversely proportional to Mn_{Ni} content x in the $Ni_{24\text{-}x}Mn_{18+x+y}Sn_{6\text{-}y}$ system. This result is consistent with the T_M (defined as $(M_s+M_f+A_s+A_f)/4$) trend observed in our experiment, indicating that △$E_{A\text{-}6M}$ can serve as a predictor of T_M.

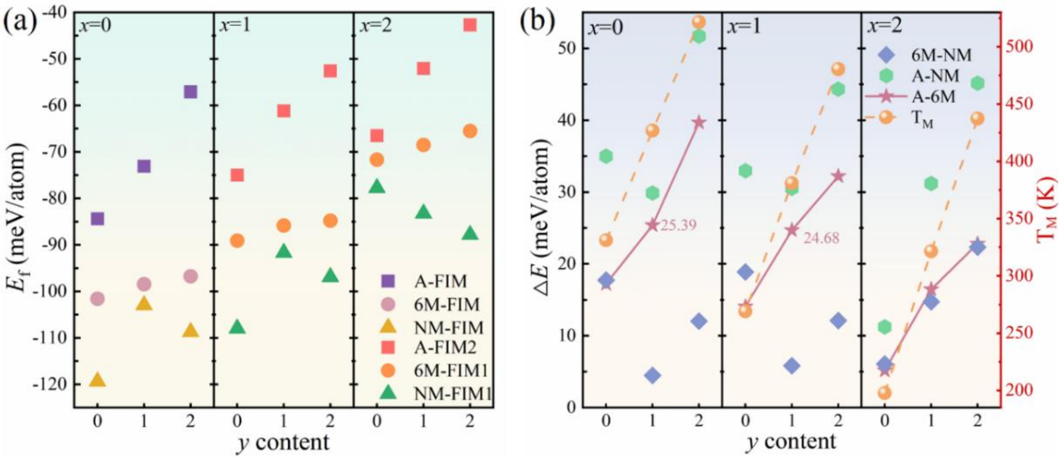

Fig. 8. (a) E_{form} of each phase and (b) △E between phases for $Ni_{24\text{-}x}Mn_{18+x+y}Sn_{6\text{-}y}$ system.

To verify the accuracy of the current calculations, EDS, DSC, XRD, and TEM analyses were carried out for the $Ni_{24\text{-}x}Mn_{18+x+y}Sn_{6\text{-}y}$ (x, y=0, 1, 2) system. The EDS results show that the experimental compositions are close to the nominal composition, as presented in Fig. 9(b). The DSC curve of Fig. 9(a) shows that the studied alloys have undergone martensitic transformations, with the T_M increasing with an increase in Mn_{Sn} content y and decreasing with an increase in Mn_{Ni} content x. However, for the $Ni_{22}Mn_{20}Sn_6$ (x=2, y=0) alloy, the martensitic transformation temperature was not detected due to the limitation of the testing temperature range for the DSC equipment (The inverse MT displayed in the DSC curve may only be a partial MT). To accurately determine the martensitic transformation temperature, we measured the magnetic-thermal (M-T) curve using a Quantum interference device (MPMS-3), as shown in the inset of Fig. 9(a). It can be seen from the M-T curve that the alloy undergoes an obvious magnetic-structure coupling phase transition, and the MT characteristic temperatures are shown in Fig. 9(b).

Then, the XRD patterns of the alloy powders were measured at room temperature, with results presented in Fig. 9(c). For $Ni_{23}Mn_{19}Sn_6$ (x=1, y=0) and $Ni_{22}Mn_{20}Sn_6$ (x=2, y=0) alloys, the diffraction patterns can be determined to be $L2_1$ austenite. It is found in the XRD pattern of $Ni_{24-x}Mn_{18+x+y}Sn_{6-y}$ ($y\neq0$) alloys exhibited a 6M martensitic structure. To further determine the crystal structure of the martensite, the $Ni_{24}Mn_{20}Sn_4$ (x=0, y=2) alloy was selected for TEM experiments. Fig. 9(d) shows the selected area electron diffraction (SAED) pattern for martensite, from which it can be seen that there are five additional state spots between the main reflection spots, characteristic of the 6M martensite structure[13,41]. Therefore, it is proved that 6M martensite does exist in the martensitic transformation sequence, which is consistent with our aforementioned result of the first-principles calculations. It is worth noting that the XRD calibration result of $Ni_{24}Mn_{18}Sn_6$ (x, y=0) alloy is 4O martensite, which is consistent with the references[42-44]. It proves that 4O martensite exists in the martensitic transformation sequence in the $Ni_{24}Mn_{18}Sn_6$ (x, y=0) alloy, therefore, the accuracy of the transformation sequence including 6M martensite for the $Ni_{24}Mn_{18}Sn_6$ alloy needs to be further confirmed.

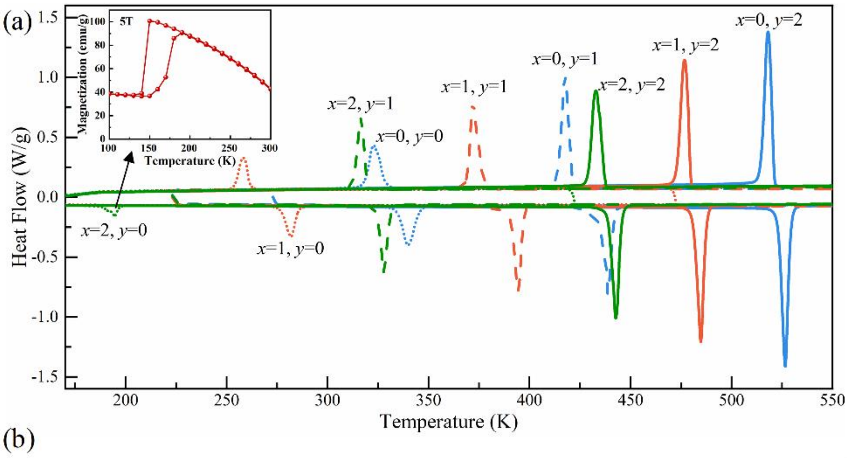

(b)

$Ni_{24-x}Mn_{18+x+y}Sn_{6-y}$ (x, y=0, 1, 2)	Computational composition	Experimental composition	Actual composition (at.%)			Temperature (K)				
			Ni	Mn	Sn	M_s	M_f	A_s	A_f	T_M
x=0, y=0	$Ni_{24}Mn_{18}Sn_6$	$Ni_{50}Mn_{37.5}Sn_{12.5}$	49.65	37.37	12.98	329.24	316.12	332.29	347.14	331.20
x=0, y=1	$Ni_{24}Mn_{19}Sn_5$	$Ni_{50}Mn_{39.58}Sn_{10.42}$	50.15	39.03	10.83	421.52	411.94	432.41	441.32	426.80
x=0, y=2	$Ni_{24}Mn_{20}Sn_4$	$Ni_{50}Mn_{41.67}Sn_{8.33}$	49.86	41.43	8.71	521.46	513.32	521.28	530.47	521.63
x=1, y=0	$Ni_{23}Mn_{19}Sn_6$	$Ni_{47.92}Mn_{39.58}Sn_{12.5}$	47.35	39.56	13.09	262.58	252.40	274.43	286.61	269.01
x=1, y=1	$Ni_{23}Mn_{20}Sn_5$	$Ni_{47.92}Mn_{41.66}Sn_{10.42}$	47.45	41.91	10.64	378.82	366.46	379.72	398.72	380.93
x=1, y=2	$Ni_{23}Mn_{21}Sn_4$	$Ni_{47.92}Mn_{43.75}Sn_{8.33}$	47.68	43.68	8.75	480.55	473.06	480.14	488.52	480.57
x=2, y=0	$Ni_{22}Mn_{20}Sn_6$	$Ni_{45.83}Mn_{41.67}Sn_{12.5}$	45.48	41.50	13.02	149.93	140.06	149.92	189.98	157.47
x=2, y=1	$Ni_{22}Mn_{21}Sn_5$	$Ni_{45.83}Mn_{43.75}Sn_{10.42}$	45.51	43.53	10.96	319.59	311.35	323.11	332.05	321.53
x=2, y=2	$Ni_{22}Mn_{22}Sn_4$	$Ni_{45.83}Mn_{45.83}Sn_{8.34}$	45.94	45.24	8.82	437.97	427.65	437.07	446.84	437.38

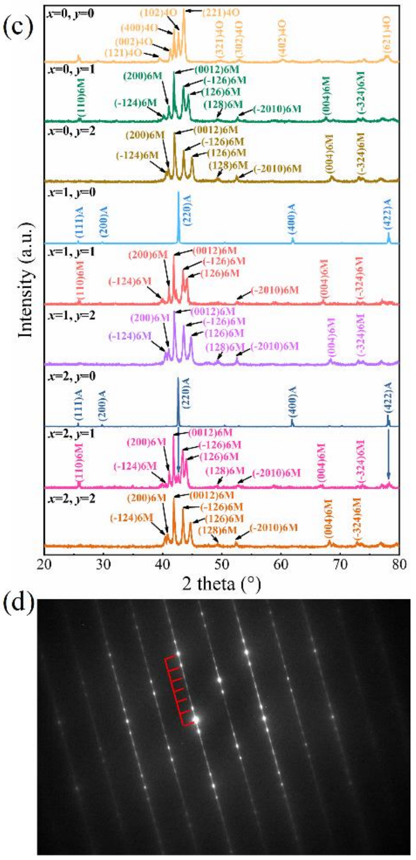

Fig. 9. (a) DSC curves of MT (Inset is M-T curve of $Ni_{22}Mn_{20}Sn_6$ alloy under magnetic field of 5T), (b) martensitic and austenitic transformation starting, finishing temperatures (M_s, M_f, A_s, and A_f), (c) room-temperature XRD patterns for $Ni_{24-x}Mn_{18+x+y}Sn_{6-y}$ (x, y=0, 1, 2) system, and (d) SAED pattern of 6M martensite for $Ni_{24}Mn_{20}Sn_4$ (x=0, y=2) alloy at room temperature.

The E_{form} of 4O martensite for the $Ni_{24}Mn_{18+y}Sn_{6-y}$ (y=0, 1, 2) alloys was calculated. According to Fig. 10, the E_{form} of 4O martensite in FIM is lower than that in FM state, indicating that 4O martensite also exists stably in FIM[45]. It is worth noting that both 4O and 6M martensites have lower E_{form} than austenite and higher than NM martensite, indicating that the alloy will undergo a phase transformation sequence: austenite–4O/6M martensite–NM martensite. However, the E_{form} of 4O and 6M martensite differs slightly. One possibility is the coexistence of 4O and 6M martensites, and some researchers have confirmed this situation in the $Ni_{45.1}Co_{6.2}Mn_{37.2}Sn_{11.5}$[46] and $Ni_{46}Co_4Mn_{38}Sn_{12}$[47] alloys through TEM analysis. The other possibility is that one type of martensite with higher E_{form} can be transformed into another more stable martensite with decrease in temperature before the occurrence of the most stable NM martensite[48]. For example, Sutou *et al.*[18] found that a three-step MT occurred in $Ni_{50}Mn_{37}Sn_{13}$ alloy during cooling through the thermomagnetization curve measured by the vibrating sample magnetometry experiment. Due to the limitation of the current experimental conditions, it remains challenging to characterize the dynamic process of the inter-transformation of the modulated martensite. We observed a relatively stable modulated martensite in the experiment at room temperature. According to the calculation results of Fig. 10, the E_{form} of 4O martensite in the $\mathrm{Ni_{24}Mn_{18}Sn_{6}}$ (x, y=0) alloy is slightly lower than that of 6M martensite, indicating that 4O martensite is relatively more stable. On the contrary, the E_{form} of 6M martensite in the $\mathrm{Ni_{24}Mn_{18+\mathit{y}}Sn_{6-\mathit{y}}}$ (x=0, y=1, 2) alloy is slightly lower than that of 4O martensite, indicating that 6M martensite is relatively more stable. This well supports the results observed in the experiment, as shown in Fig. 9(c).

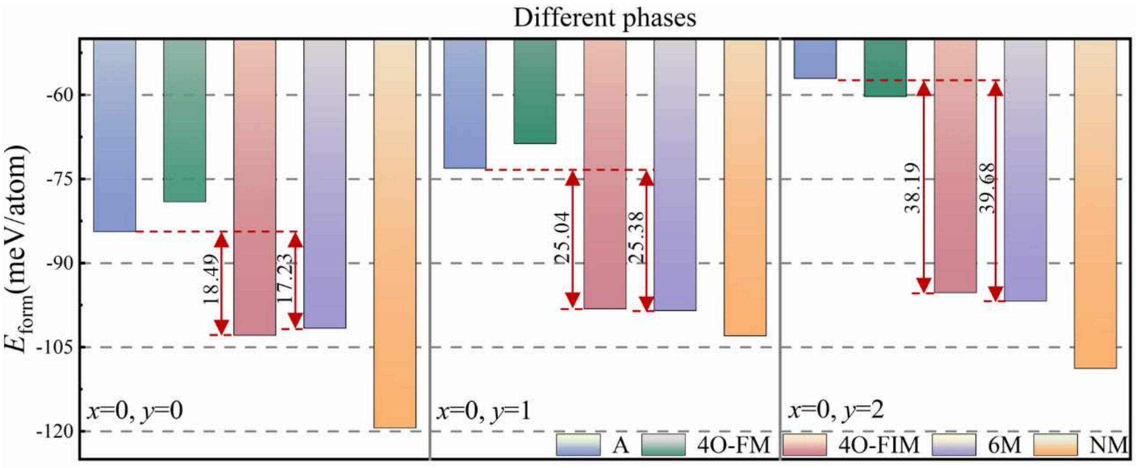

Fig. 10. E_{form} of A, 6M, and NM phases in the most stable state and 4O in ferromagnetic and ferrimagnetic states for $\mathrm{Ni_{24-\mathit{x}}Mn_{18+\mathit{x}+\mathit{y}}Sn_{6-\mathit{y}}}$ (x=0, y=0, 1, 2) alloys.

3.4. Kinetic behavior of martensitic transformation

The austenite to the martensite, on the one hand, needs a sufficient free energy difference between the new and parent phase, which acts as the driving force for the transformation; on the other hand, the phase transformation barrier must be overcome. The $\triangle E_{\mathrm{A\text{-}6M}}$ obtained through first-principles calculations in section 3.3 increases with the increasing $\mathrm{Mn_{Sn}}$ content y and decreases with the increasing $\mathrm{Mn_{Ni}}$ content x, which is the thermodynamic reason why it is observed that the T_M increases with increasing y and decreases with increasing x. To give in-depth insight into the theoretical basis for the MT behavior, we will analyze why the T_M varies with the composition from the perspective of non-isothermal kinetics.

Fig. 11 presents the DSC curves and activation energy calculations at different rates from 5 to 20 K/min for the $\mathrm{Ni_{24-\mathit{x}}Mn_{18+\mathit{x}+\mathit{y}}Sn_{6-\mathit{y}}}$ (x=0, y=0, 1, 2, and x=1, 2, y=2) alloys. As shown in Fig. 11(a), the reverse martensitic transformation temperature increases and the transformation temperature range widens with increasing heating rate. This phenomenon is because a higher heating rate shortens the incubation period, reduces the nucleation degree of austenite, and promotes the phase transformation to a higher temperature, thereby prolonging the transformation time and broadening the transformation temperature range. According to the DSC curves of different rates, the Q value can be obtained by the Kissinger equation (Eq. 3-5) as follows:[49,50]

$$\frac{\mathrm{d}\left(\ln\left(\frac{\beta}{T_p^2}\right)\right)}{\mathrm{d}\left(\frac{1}{T_p}\right)} = -\frac{\mathrm{Q}}{\mathrm{R}} \tag{3-5}$$

Where β is the heating rate, T_p is the peak temperature of the heating curve, and R is the universal gas constant (R = 8.314 J/mol). The slope curve obtained by fitting $\ln(\beta/T_p^2)$ and $1000/T_p$ is shown in Fig. 11(b). The slope increases with increasing y and decreases with increasing x. The results show that the Q for $Ni_{24\text{-}x}Mn_{18+x+y}Sn_{6\text{-}y}$ (x=0, y=0, 1, 2) and $Ni_{24\text{-}x}Mn_{18+x+y}Sn_{6\text{-}y}$ (x=1, 2, y= 2) alloys is 367.98, 536.25, 966.25, 858.75, and 548.23 kJ/mol, respectively.

The Q value is a critical parameter that describes the kinetic characteristics and can reflect the difficulty degree of phase transformation. A higher Q value indicates a higher energy barrier that must be overcome, requiring more energy and leading to a slower rate of transformation. This in turn results in a higher phase transition temperature, as a higher temperature is needed to overcome the higher energy barrier and promote the occurrence of phase transition. This is another factor that the martensitic transformation temperature observed in the experiments ascends with increasing Mn_{Sn} content and descends with increasing Mn_{Ni} content.

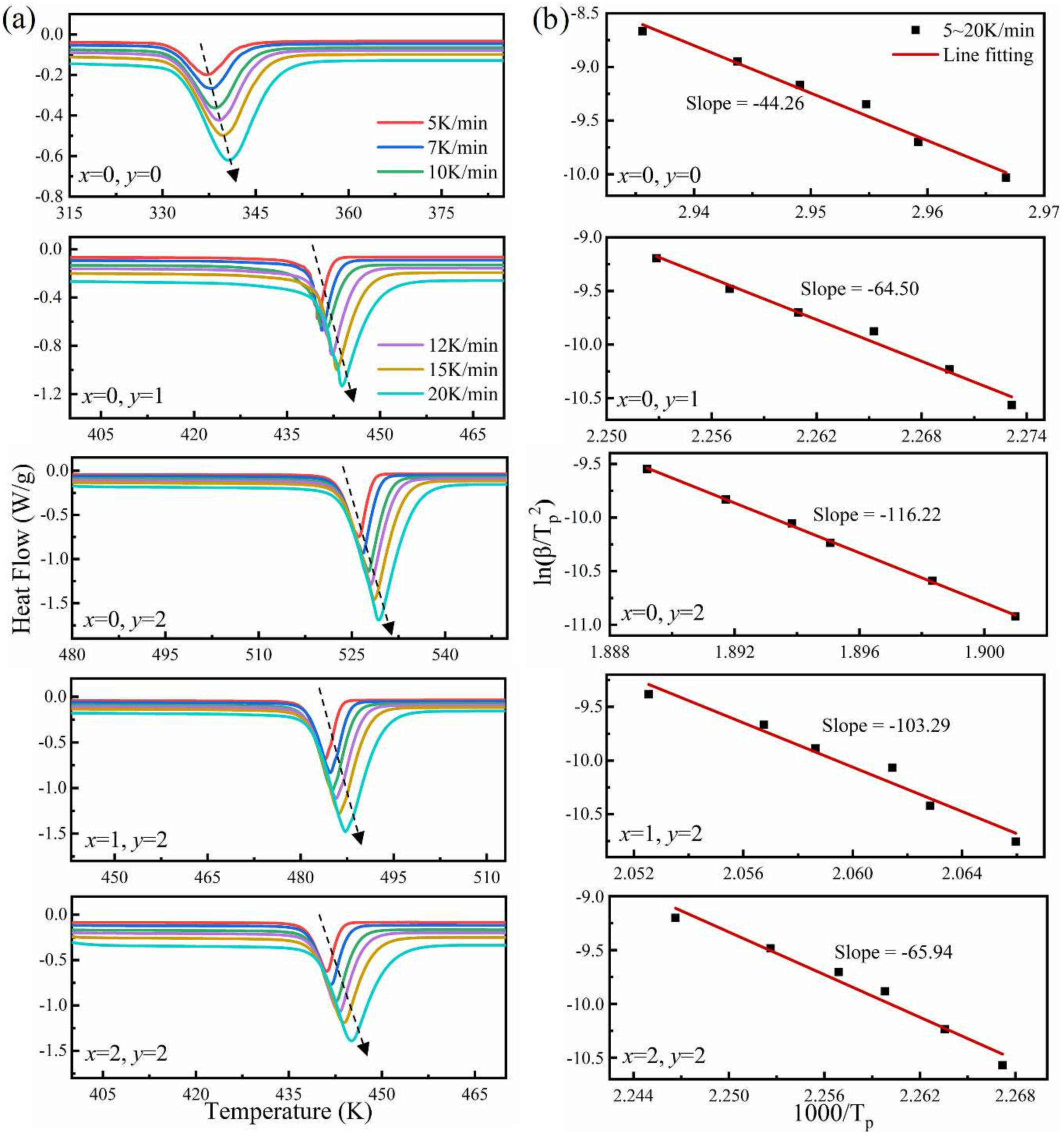

Fig. 11. (a) DSC curves and (b) variation of $\ln(\beta/T_p^2)$ with $1000/T_p$ at 5~20K/min heating rates of $Ni_{24\text{-}x}Mn_{18+x+y}Sn_{6\text{-}y}$ (x=0, y=0, 1, 2, and x=1, 2, y=2) alloys.

3.5. Electronic structure

Fig. 12 illustrates the electronic total density of states (TDOS) of A, 6M, and NM phases for the $Ni_{24\text{-}x}Mn_{18+x+y}Sn_{6\text{-}y}$ system to explore the origin of MT and magnetic properties. The spin-down TDOS of the austenite has a small peak near the Fermi level (E_F), which diminishes the phase's stability at low temperature[51], and is considered to be the key factor to trigger MT. During the transformation from austenite to martensite, the density peak for the spin-down TDOS near the E_F splits, causing the E_F shift to the pseudo-energy gap or even in the pseudopotential valley, such a change of the electronic structure makes the low-temperature martensites (6M and NM) more stable than austenite, known as the band Jahn-Teller effect[52]. In the $Ni_{22}Mn_{20}Sn_6$ (x=2, y=0) alloy, the difference in the total DOS between the austenite and 6M or NM martensite shows little variation at the E_F, making the band Jahn-Teller effect less noticeable, which may be related to its lower T_M.

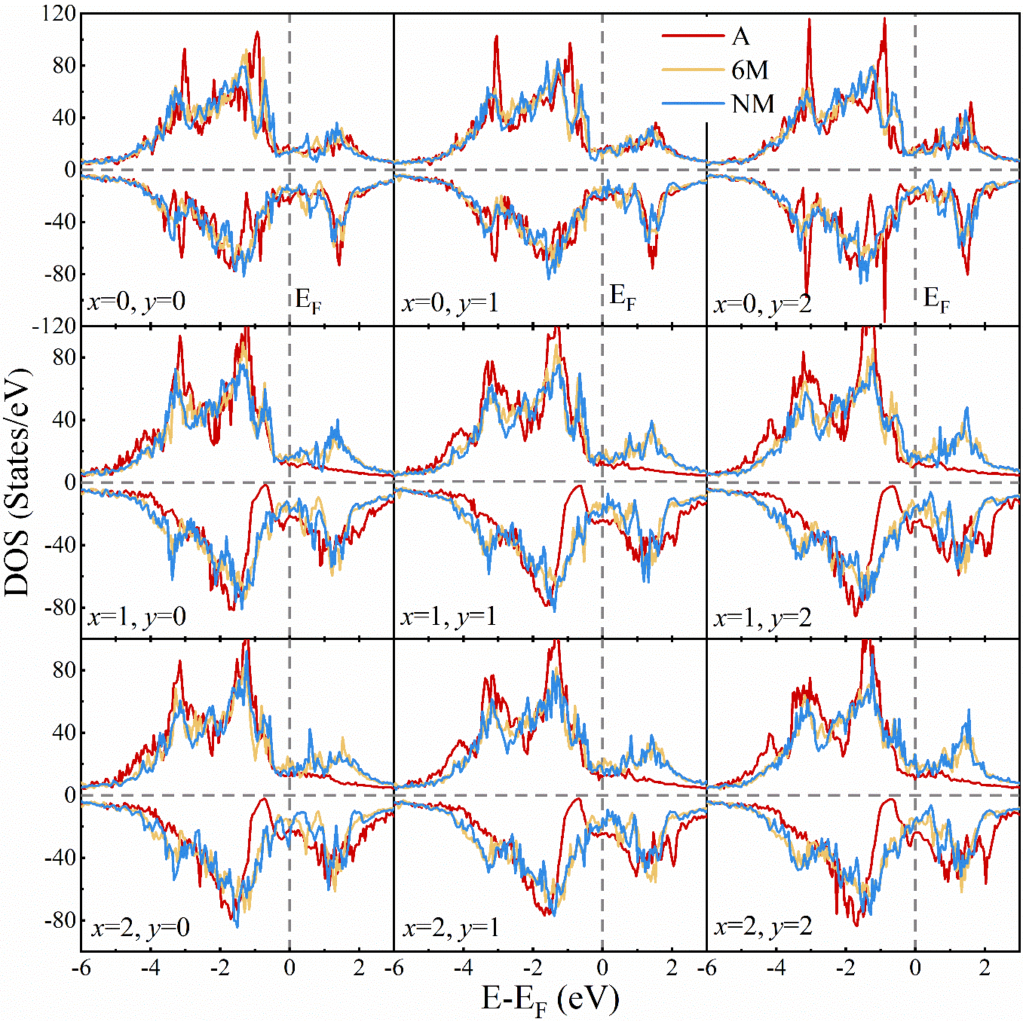

Fig. 12. Total density of states (TDOS) near Fermi energy (E_F) of $Ni_{24-x}Mn_{18+x+y}Sn_{6-y}$ alloys in austenite, 6M, and NM martensites. E_F stands for zero energy.

There are two prominent peaks around -3eV and -1eV in the spin-up TDOS, which result from the strong 3*d* electron interaction between Ni and Mn atoms. In the Mn-excess Ni and Sn-deficient alloys, there is a distinct pseudopotential valley at -0.4 eV to -1.3 eV of spin-down TDOS, indicating the presence of a strong covalent bond in austenite. To further explore the essential reason for covalent bonds formation, taking the $Ni_{23}Mn_{19}Sn_6$ (x=1, y=0) alloy as an example, the partial density of states (PDOS) was calculated, as depicted in Fig. 13. In comparison, the resonance between the minority electronic states of Ni and Mn_{Ni} near the pseudo gap is more obvious than that between Ni and other atoms, implying that the formation of covalent bonds primarily arises from this interaction.

The atomic magnetic moment is sensitive to the arrangement of valence electrons, and the magnetism is mainly contributed by 3*d* electrons in NiMn-based Heusler alloys. As depicted in Fig. 13(a_1)-(c_1), the spin-up and spin-down 3*d* electron arrangements of Ni atoms are similar in the austenite, 6M, and NM phases, resulting in small magnetic moments of Ni atoms (-0.035~0.779 μ_B), consistent with the calculated results in Fig. 7(a). The spin-up electrons of the Mn_{Mn} in the three phases are mainly distributed below the E_F, and the spin-down electrons are mostly distributed above the E_F, as depicted in Fig. 13(a_2)-(c_2). This uneven distribution of valence electrons leads to a large magnetic moment of Mn_{Mn} (-3.635~3.750 μ_B). Differently, the spin-up electrons of Mn_{Ni} atoms are mainly distributed above the E_F, and the spin-down electrons are mainly distributed below the E_F, as illustrated in Fig. 13(a_3)-(c_3). It demonstrates that the magnetic moments of Mn_{Mn} and Mn_{Ni} in the three phases are antiparallel. From Fig. 13(a_2)-(a_4), the arrangement of 3*d* electrons of Mn_{Sn} and Mn_{Mn} atoms in austenite is the same, but totally different from that of Mn_{Ni}, which means that the magnetic moments of Mn_{Mn} and Mn_{Ni} are arranged in parallel and antiparallel with Mn_{Sn} atoms, respectively. It is further confirmed that the austenite for the $Ni_{24-x}Mn_{18+x+y}Sn_{6-y}$ (x=1, 2) alloys exists stably in the FIM2 state. Nevertheless, as shown in Fig. 13(b_4)-(c_4), the arrangement of 3*d* electrons of Mn_{Sn} and Mn_{Ni} atoms in the 6M and NM martensites is the same, but different from that of Mn_{Mn}, indicating that the magnetic moments of Mn_{Sn} and Mn_{Ni} are both arranged antiparallel to that of the Mn_{Mn} atoms. It proves that the 6M and NM martensites exist stably in the FIM1 state for Mn-excess Ni and Sn-deficient alloys. The above results show how the electron arrangement of Mn_{Sn} determines the magnetic state, leading to a large $\triangle M$ during MT, which is also the essential reason for the magnetic-structure coupling transition of the $Ni_{24-x}Mn_{18+x+y}Sn_{6-y}$ (x=1, 2) alloys.

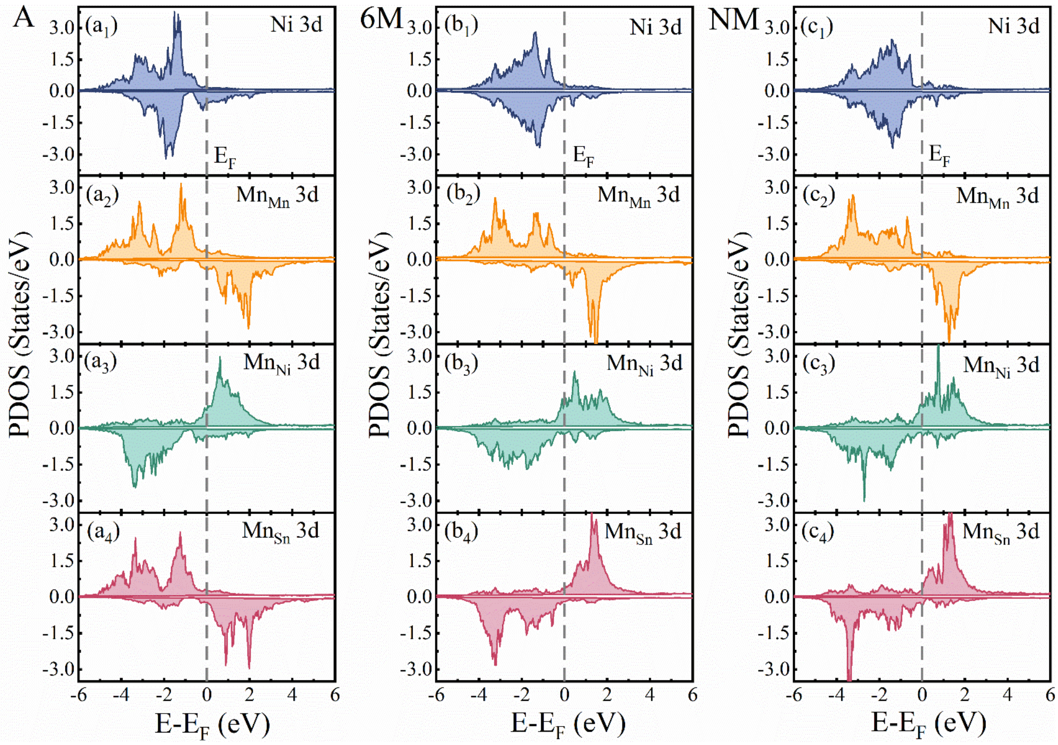

Fig. 13. Partial density of states (PDOS) of austenite, 6M, and NM martensites for Ni$_{23}$Mn$_{19}$Sn$_6$ (x=1, y=0).

4. Conclusions

In the present work, the first-principles calculations in combination with experiments method were used to systematically investigate the phase stability, martensitic transformation, kinetics, and magnetic properties of the Ni$_{24-x}$Mn$_{18+x+y}$Sn$_{6-y}$ (x, y=0, 1, 2) system. The main conclusions are summarized as follows:

(1) The austenite, 6M, and NM martensites present the FIM state for the Mn-excess Sn-deficient system. For the Mn-excess Ni and Sn-deficient system, austenite is stable in the FIM2 state, whereas the FIM1 state is the most thermodynamically stable state for the 6M and NM martensites.

(2) The formation energy of each phase is obtained and mapped onto the ternary phase diagram. The formation energy of the austenite increases with the increasing Mn content, and the fitting equation is $E_{\text{form-A}}$=507.358X_{Mn}-274.126. And the formation energy of the 6M martensite shows a linear decrease with an increase in the Ni content, the fitting equation is $E_{\text{form-6M}}$=-728.484X_{Ni}+264.374.

(3) The changing trend of the lattice parameters for each phase is mainly affected by the atomic radius in the studied alloy system. The ternary phase diagram of the total magnetic moment of each phase is established. The total magnetic moment of austenite decreases with the increasing Mn$_{\text{Sn}}$

content y in the $Ni_{24-x}Mn_{18+x+y}Sn_{6-y}$ (x=0) alloys, while it changes oppositely with the increasing y in the $Ni_{24-x}Mn_{18+x+y}Sn_{6-y}$ (x=1, 2) alloys. In addition, the total magnetic moment of austenite decreases with the increasing x in $Ni_{24-x}Mn_{18+x+y}Sn_{6-y}$ (x =1, 2) alloy. The total magnetic moments of 6M and NM martensites both decrease with the increase in Mn content, and the fitting formulas are $Mag_{6M}=-15.905X_{Mn}+7.902$ and $Mag_{NM}=-14.781X_{Mn}+7.411$, respectively. Mn atoms are the primary contributors to the total magnetic moment, and the trend of the total magnetic moment with composition also depends on the variation of Mn atomic magnetic moment.

(4) Combined with formation energy calculations and experimental results, the possible martensite transformation sequence including 6M in the process of cooling and heating as $Austenite^{FIM}\leftrightarrow 6M^{FIM}\leftrightarrow NM^{FIM}$ for the $Ni_{24-x}Mn_{18+x+y}Sn_{6-y}$ (x=0) alloys and the transformation path corresponds to $Austenite^{FIM2}\leftrightarrow 6M^{FIM1}\leftrightarrow NM^{FIM1}$ for the $Ni_{24-x}Mn_{18+x+y}Sn_{6-y}$ (x=1, 2) alloys.

(5) From the perspectives of formation energy difference ($\triangle E_{A\text{-}6M}$) and activation energy (Q), the reason for the change of martensite transformation temperature with composition is explained. A decrease in Mn_{Ni} content x or an increase in Mn_{Sn} content y corresponds to a rise in T_M.

Acknowledgments

This work is financially supported by the National Natural Science Foundation of China (Grant No. 51771044), the Natural Science Foundation of Hebei Province (No. E2019501061), the Performance subsidy fund for Key Laboratory of Dielectric and Electrolyte Functional Material Hebei (No. 22567627H), the Fundamental Research Funds for the Central Universities (No. N2223025), 2023 Hebei Provincial doctoral candidate Innovation Ability training funding project (CXZZBS2023165), and the Programme of Introducing Talents of Discipline Innovation to Universities 2.0 (the 111 Project of China 2.0, No. BP0719037). Thanks to the support of the Shanxi Supercomputing Center of China, the calculations for this work were performed on TianHe-2. This project is supported by the China Scholarship Council (CSC).

Author contributions

Bai J conceived and coordinated the project, and were responsible for the infrastructure and project direction. Zhang Y and Guo KL conducted the theoretical calculations. Xu JX, Gu JL, Morley N, Gao QZ, Zhang YD, Esling C, Zhao X and Zuo L contributed to data analysis and interpretation. Zhang Y wrote the manuscript. All authors contributed to the general discussion.(删)

Conflict of Interest The authors state that there are no conflicts of interest to disclose.

Reference

[1] Kainuma R, Imano Y, Ito W, Morito H, Sutou Y, Oikawa K, Fujita A, Ishida K, Okamoto S, Kitakami O, Kanomata T. Metamagnetic shape memory effect in a Heusler-type polycrystalline alloy. Appl. Phys. Lett. 2006;88(19):192513.

[2] Li Z, Jing C, Zhang HL, Qiao YF, Cao SX, Zhang JC, Sun L. A considerable metamagnetic shape memory effect without any prestrain in $Ni_{46}Cu_4Mn_{38}Sn_{12}$ Heusler alloy. J. Appl. Phys. 2009;106:083908.

[3] Li ZB, Dong SY, Li ZZ, Yang B, Liu F, Sánchez-Valdés CF, Sánchez Llamazares JL, Zhang YD, Esling C, Zhao X, Zuo L. Giant low-field magnetocaloric effect in Si alloyed Ni-Co-Mn-In alloys. Scr. Mater. 2019;159:113-118.

[4] Krenke T, Duman E, Acet M, Wassermann EF, Moya X, Mañosa L, Planes A. Inverse magnetocaloric effect in ferromagnetic Ni-Mn-Sn alloys. Nat. Mater. 2005;4(6):450-454.

[5] Shen Y, Sun W, Wei ZY, Shen Q, Zhang YF, Liu J. Orientation dependent elastocaloric effect in directionally solidified Ni-Mn-Sn alloys. Scr. Mater. 2019;163:14-18.

[6] Sun W, Liu J, Lu BF, Li Y, Yan A. Large elastocaloric effect at small transformation strain in $Ni_{45}Mn_{44}Sn_{11}$ metamagnetic shape memory alloys. Scr. Mater. 2016;114:1-4.

[7] Yu SY, Ma L, Liu GD, Liu ZH, Chen JL, Cao ZX, Wu GH, Zhang B, Zhang XX. Magnetic field-induced martensitic transformation and large magnetoresistance in NiCoMnSb alloys. Appl. Phys. Lett. 2007;90(24):242501.

[8] Li ZB, Hu W, Chen FH, Zhang MG, Li ZZ, Yang B, Zhao X, Zuo L. Large magnetoresistance in a directionally solidified $Ni_{44.5}Co_{5.1}Mn_{37.1}In_{13.3}$ magnetic shape memory alloy. J. Magn. Magn. Mater. 2018;452:249-252.

[9] Qu YH, Cong DY, Li SH, Gui WY, Nie ZH, Zhang MH, Ren Y, Wang YD. Simultaneously achieved large reversible elastocaloric and magnetocaloric effects and their coupling in a magnetic shape memory alloy. Acta Mater. 2018;151:41-55.

[10] Koyama K, Watanabe K, Kanomata T, Kainuma R, Oikawa K, Ishida K. Observation of field-induced reverse transformation in ferromagnetic shape memory alloy $Ni_{50}Mn_{36}Sn_{14}$. Appl. Phys. Lett. 2016;88(13):132505.

[11] Liu FS, Wang QB, Li SP, Ao WQ, Li JQ. The martensitic transition and magnetocaloric properties of $Ni_{51}Mn_{49-x}Sn_x$. Physica B. 2013;412:74-78.

[12] Zhang GY, Li D, Liu C, Li ZB, Yang B, Yan HL, Zhao X, Zuo L. Giant low-field actuated caloric effects in a textured $Ni_{43}Mn_{47}Sn_{10}$ alloy. Scr. Mater. 2021;201:113947.

[13] Huang L, Cong DY, Ma L, Nie ZH, Wang MG, Wang ZL, Suo HL, Ren Y, Wang YD. Large

magnetic entropy change and magnetoresistance in a $Ni_{41}Co_9Mn_{40}Sn_{10}$ magnetic shape memory alloy. J. Alloys Compd. 2015;647:1081-1085.

[14] Li FQ, Qu YH, Yan HL, Chen Z, Cong DY, Sun XM, Li SH, Wang YD. Giant tensile superelasticity originating from two-step phase transformation in a Ni-Mn-Sn-Fe magnetic microwire. Appl. Phys. Lett. 2018;113(11):112402.

[15] Huang L, Cong DY, Ren Y, Wei KX, Wang YD. Effect of Al substitution on the magnetocaloric properties of Ni-Co-Mn-Sn multifunctional alloys. Intermetallics. 2020;119:106706.

[16] Sarkar SK, Ahlawat S, Kaushik SD, Babu PD, Sen D, Honecker D, Biswas A. Magnetic ordering of the martensite phase in Ni-Co-Mn-Sn-based ferromagnetic shape memory alloys. J. Phys.: Condens. Matter. 2020;32:115801.

[17] Tian HF, Lu JB, Ma L, Shi HL, Yang HX, Wu GH, Li JQ. Martensitic transformation and magnetic domains in $Mn_{50}Ni_{40}Sn_{10}$ studied by in-situ transmission electron microscopy. J. Appl. Phys. 2012;112(3):033904.

[18] Sutou Y, Imano Y, Koeda N, Omori T, Kainuma R, Ishida K, Oikawa K. Magnetic and martensitic transformations of NiMnX(X=In, Sn, Sb) ferromagnetic shape memory alloys. Appl. Phys. Lett. 2004;85(19):4358-4360.

[19] Yan HL, Zhang YD, Xu N, Senyshyn A, Brokmeier HG, Esling C, Zhao X, Zuo L. Crystal structure determination of incommensurate modulated martensite in Ni-Mn-In Heusler alloys. Acta Mater. 2015;88:375-388.

[20] Chernenko VA, Cesari E, Khovailo V, Pons J, Seguí C, Takagi T. Intermartensitic phase transformations in Ni-Mn- Ga studied under magnetic field. J. Magn.Mater. 2005;871:290-291.

[21] Mehaddene T, Neuhaus J, Petry W, Hradil K, Bourges P, Hiess A. Interplay of structural instability and lattice dynamics in Ni_2MnAl. Phys. Rev. B. 2008;78(10):104110.

[22] Yang LH, Zhang H, Hu FX, Sun JR, Pan LQ, Shen BG. Magnetocaloric effect and martensitic transition in $Ni_{50}Mn_{36-x}Co_xSn_{14}$. J. Alloys Comp. 2014;588:46-48.

[23] Kanomata T, Umetsu RY, Ohtsuki K, Shoji T, Endo K, Fukushima K, Nishihara H, Ito W, Adachi Y, Miura T, Oikawa K, Kainuma R, Ziebeck KRA. Magnetic phase diagram of $Ni_2Mn_{1.44-x}Cu_xSn_{0.56}$ shape memory alloys. J. Alloys Comp. 2014;590:221-226.

[24] Hu QM, Li CM, Yang R, Kulkova SE, Bazhanov DI, Johansson B, Vitos L. Site occupancy, magnetic moments, and elastic constants of off-stoichiometric Ni_2MnGa from first-principles calculations. Phys. Rev. B. 2009;79(14):144112.

[25] Li CM, Luo HB, Hu QM, Yang R, Johansson B, Vitos L. Site preference and elastic properties of Fe-, Co-, and Cu-doped Ni_2MnGa shape memory alloys from first principles. Phys. Rev. B. 2011;84(2):024206.

[26] Luo HB, Hu QM, Li CM, Yang R, Johansson B, Vitos L. Phase stability of $Ni_2(Mn_{1-x}Fe_x)Ga$: A

first-principles study. Phys. Rev. B. 2012;86(2):024427.

[27] Inaekyan K, Brailovski V, Prokoshkin S, Korotitskiy A, Glezer A. Characterization of amorphous and nanocrystalline Ti-Ni-based shape memory alloys. J. Alloys Comp. 2009;473(1-2):71-78.

[28] Zhou ZN, Yang L, Li RC, Li J, Hu QD, Li JG. Martensitic transformations and kinetics in Ni-Mn-In-Mg shape memory alloys. Intermetallics. 2018;92:49-54.

[29] Kresse G, Joubert D. From ultrasoft pseudopotentials to the projector augmented-wave method. Phys. Rev. B. 1999;59(3):1758-1775.

[30] Hafner J. Atomic-scale computational materials science. Acta Mater. 2000;48(1):71-92.

[31] Blöchl PE. Projector augmented-wave method. Phys. Rev. B. 1994;50(24):17953-17979.

[32] Kern G, Kresse G, Hafner J. Ab initio calculation of the lattice dynamics and phase diagram of boron nitride. Phys. Rev. B. 1999;59(13):8551-8559.

[33] Perdew JP, Burke K, Ernzerhof M. Generalized gradient approximation made simple. Phys. Rev. Lett. 1996;77(18):3865-3868.

[34] Monkhorst HJ, Pack JD. Special points for Brillouin-zone integrations. Phys. Rev. B. 1976;13(12):5188-5192.

[35] Lin CQ, Yan HL, Zhang YD, Esling C, Zhao X, Zuo L. Crystal structure of modulated martensite and crystallographic correlations between martensite variants of $Ni_{50}Mn_{38}Sn_{12}$ alloy. J. Appl. Crystallography. 2016;49:1276-1283.

[36] Bai J. Wang JL, Shi SF, Raulot JM, Zhang YD, Esling C, Zhao X, Zuo L. Complete martensitic transformation sequence and magnetic properties of non-stoichiometric $Ni_2Mn_{1.2}Ga_{0.8}$ alloy by first-principles calculations. J. Magn. Magn. Mater. 2019;473:360-364.

[37] Yamada T, Kunitomi N, Nakal Y, Cox DE, Shirane G. Magnetic structure of α-Mn. J. Phys. Soc. Jpn. 1970;28(3):615-627.

[38] Ghosh S, Ghosh S. Understanding the origin of the magnetocaloric effects in substitutional Ni-Mn-Sb-Z (Z=Fe,Co,Cu) compounds: Insights from first-principles calculations. Phys. Rev. B. 2020;101(2):024109.

[39] Muthu SE, Rao NVR, Raja MM, Kumar DMR, Radheep DM, Arumugam S. Influence of Ni/Mn concentration on the structural, magnetic and magnetocaloric properties in $Ni_{50-x}Mn_{37+x}Sn_{13}$ Heusler alloys. J. Phys. D: Appl. Phys. 2010;43(42):425002.

[40] Miroshkina ON, Eggert B, Lill J, Beckmann B, Koch D, Hu MY, Lojewski T, Rauls S, Scheibel F, Taubel A, Šob M, Ollefs K, Gutfleisch O, Wende H, Gruner ME, Friák M. Impact of magnetic and antisite disorder on the vibrational densities of states in Ni_2MnSn Heusler alloys. Phys. Rev. B. 2022;106(21): 214302.

[41] Li ZB, Jiang YW, Li ZZ, Valde´s CFS, Llamazares JLS, Yang B, Zhang YD, Esling C, Zhao X, Zuo L. Phase transition and magnetocaloric properties of $Mn_{50}Ni_{42-x}Co_xSn_8$ $(0 \leq x \leq 10)$ melt-

spun ribbons. IUCrJ. 2018;5:54-66.

[42] Maziarz W, Czaja P, Szczerba MJ, Lityn´ska-Dobrzyn´ska L, Czeppe T, Dutkiewicz J. Influence of Ni/Mn concentration ratio on microstructure and martensitic transformation in melt spun Ni-Mn-Sn Heusler alloy ribbons. J. Alloys Comp. 2014;615:S173-S177.

[43] Chulist R, Czaja P. On the role of atomic shuffling in the 4O, 4M and 8M martensite structures in Ni-Mn-Sn single crystal. Scr. Mater. 2020;189:106-111.

[44] Sokolovskiy VV, Buchelnikov VD, Zagrebin MA, Enter P, Sahoo S, Ogura M. First-principles investigation of chemical and structural disorder in magnetic $Ni_2Mn_{1+x}Sn_{1-x}$ Heusler alloys. Phys. Rev. B. 2012;86(13):134418.

[45] Friák M, Zelený M, Mazalová M, Miháliková I, Turek, I, Kaštil, J, Kamarád J, Míšek M, Arnold Z, Schneeweiss O, Šob M. The impact of disorder on the 4O-martensite of Ni-Mn-Sn Heusler alloy. Intermetallics. 2022;151:107708.

[46] Czaja P, Chulist R, Szlezynger M, Fitta M, Maziarz W. Multiphase microstructure and extended martensitic phase transformation in directionally solidified and heat treated $Ni_{44}Co_6Mn_{39}Sn_{11}$ metamagnetic shape memory alloy. Proceedings of the International Conference on Martensitic Transformations: Chicago, 2018: 263-267.

[47] Miyakawa T, Ito T, Xu X, Omori T, Kainuma R. Martensitic transformation near room temperature and hysteresis in $(Ni\text{-}Co)_{50}$-Mn-Sn metamagnetic shape memory alloys. J. Alloys Comp. 2022;913:165136.

[48] Çakır A, Righi L, Albertini F, Acet M, Farle M. Intermartensitic transitions and phase stability in $Ni_{50}Mn_{50-x}Sn_x$ Heusler alloys. Acta Mater. 2015;99:140-149.

[49] Fang H, Wong B, Bai Y. Kinetic modelling of thermophysical properties of shape memory alloys during phase transformation. Const. Build. Mater. 2017;131:146-155.

[50] Kissinger HE. Reaction Kinetics in Differential Thermal Analysis. Anal. Chem. 1957;29(11):1702–1706.

[51] Li CM, Luo HB, Hu QM, Yang R, Johansson B, Vitos L. Role of magnetic and atomic ordering in the martensitic transformation of Ni-Mn-In from a first-principles study. Phys. Rev. B. 2012;86(21):214205.

[52] Barman SR, Banik S, Chakrabarti A. Structural and electronic properties ofNi_2MnGa. Phys. Rev. B. 2005;72(18):184410.